

Measuring the Particle Packing of L-Glutamic Acid Crystals through X-ray Computed Tomography for Understanding Powder Flow and Consolidation Behavior

T. D. Turner,* P. Gajjar, I. S. Fragkopoulos, J. Carr, T. T. H. Nguyen, D. Hooper, F. Clarke, N. Dawson, P. J. Withers, and K. J. Roberts



Cite This: *Cryst. Growth Des.* 2020, 20, 4252–4263



Read Online

ACCESS |



Metrics & More

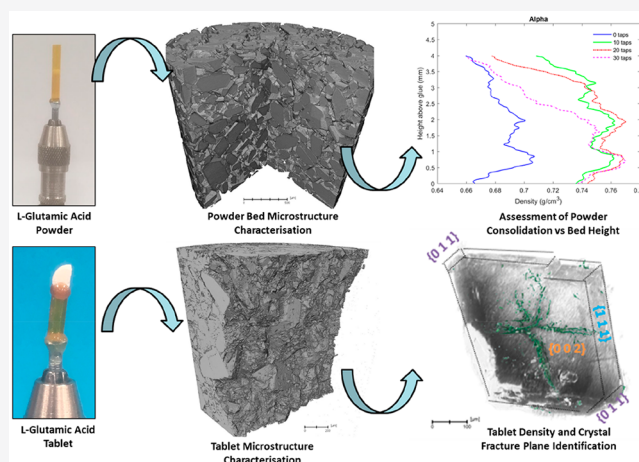


Article Recommendations



Supporting Information

ABSTRACT: The morphology of free-flowed and gravity consolidated crystal powder beds of the alpha and beta polymorphic forms of L-glutamic acid, together with a detailed analysis of particle density and microstructure within alpha form tablets using state-of-the-art X-ray computed tomography (XCT), is presented. The Carr's index is measured to be 19.7 and 35.2 for the bulk powders of the prismatic alpha form and needle-like beta form, respectively, revealing the alpha forms increased powder flowability versus the beta form. XCT reveals the alpha form consolidates under gravity more efficiently than beta, where the final measured bed density of the alpha form is 0.724 g/cm³ compared to 0.248 g/cm³ for the beta form, which is found to be caused by the inability of the beta particles to pack efficiently along their needle axis. Tableting studies reveal that the alpha form consolidates into compacts of intermediate tensile strength, whereas the beta form cannot be compacted under these conditions. XCT analysis of tablets formed from α -form crystals reveals two discrete density regimes, one low-density region of fine powder which accounts for 53.8% of the compact, and high-density regions of largely intact single crystals which account for 44.2% of the compact. Further analysis of the tablet microstructure reveals that the crystal particles are generally orientated with their basal {0 0 1} plane, normal to the compaction force and that small microcracks which appear within the particles generally occur perpendicular to the surface and are orientated through possible {1 1 0} and {1 0 1} fracture planes. XCT also reveals evidence for incipient transformation between the meta-stable alpha to stable beta phase at concentrations below that detected using laboratory X-ray diffraction. The results show that XCT can accurately measure the extent of tapping induced densification and reveals the powder bed mesostructure characteristics and tablet microstructure for the two polymorphic forms of alpha and beta L-glutamic acid.



1. INTRODUCTION

The quality by design paradigm^{1,2} for pharmaceutical product development and manufacture requires a number of robust computational models and workflows which can be used to determine the downstream processability of a chosen product formulation based on the material properties of its constituent ingredients. Quantification of both the mechanical deformation properties of a pharmaceutical material and the resulting performance attributes during processing can be a critical step in moving toward a digital design workspace.^{3–5} The habit, mechanical, and surface properties of a crystalline solid can impact strongly upon a number of process unit operations, in particular, the compactability and flowability of bulk powders. The compactability of a powder depends on the particle size, shape, and particle surface properties. During compaction, movement, breakage, and interactions can occur between

individual particles and between particles and process equipment internals.⁶ Hence, the density of the powder within the powder bed can change, leading in turn to variations in the local material properties within the tablet. All this can impact upon the content uniformity of the product and, in extreme cases, result in variable dissolution profiles with a concomitant impact on the safety and efficacy of the drug product leading to product failures and increased production costs.

Received: November 11, 2019

Revised: May 7, 2020

Published: May 12, 2020



X-ray computed tomography (XCT) has been employed for use in many industrial applications but has potential utility in the pharmaceutical industry for studying particle processing behavior such as tableting. As X-rays pass through a sample, their attenuation is related to the atomic weight of the material and the amount of material, with the attenuation being given by the Beer–Lambert law.⁷ The transmitted X-rays can be recorded forming a two-dimensional (2D) projection radiograph. XCT works by collecting a set of radiographs as the sample is rotated about 360°, from which a virtual three-dimensional (3D) representation of the sample can be reconstructed using a mathematical algorithm.^{8–10} The virtual volume allows nondestructive analysis of the sample, and hence XCT has been utilized in visualizing and quantitatively investigating powder packing and particle movement during compaction,¹¹ measuring density variations in tablets,^{12–14} studying internal tablet defects such as crack propagation,^{15,16} and understanding the structural features of solid dosage forms as well as the changes to them during manufacturing, handling, and storage.¹⁷ Recent advances in both X-ray source and detector technologies, in particular, the utilization of X-ray optics in laboratory systems, has provided increased spatial resolution to 0.6 μm and enhanced contrast,¹⁸ allowing the quantification of the structure of tableting grade lactose.¹⁹ XCT has been previously used in combination with X-ray diffraction to reveal information about particle orientation in stirred batch crystallizers to reveal the preferential orientation of crystallites as a function of crystallization process parameters.^{20,21} XCT has also been exploited in the area of controlled drug delivery for exploring the relationships between delivery device, formulation, structure, and performance.^{22–25}

In this study L-glutamic acid (LGA) is used as a model compound to study the impact of variation in the polymorphic form and crystal habit on the consolidation behavior of the material. LGA has a comparatively simple molecular structure that crystallizes in two polymorphic forms, the metastable α -form and the stable β -form.^{26,27} In aqueous solution, the metastable α -form crystallizes at high cooling rates, whereas the stable β -form crystallizes at lower cooling rates.²⁶ The polymorphic transformation between these two forms is known to be monotropic and solvent-mediated.^{28–32} The metastable α -form crystallizes as prisms, while the stable β -form crystallizes as needle-like particles. Although the α -form is metastable, it is very stable to transformation under laboratory storage conditions. Molecular modeling studies have found that the stability of these two polymorphic forms is size dependent.^{33,34}

The specific aim of the work presented here is to further understand how organic crystalline materials of different crystal polymorphic form and morphology consolidate to form powder beds. This ultimately impacts the ability of a material to form compacts, which is of particular importance to the pharmaceutical industry where the favored route to an oral dosage form is via direct compression of the formulation into tablets.^{35,36} This study utilizes XCT to probe the impact of particle habit and material mechanical properties of the alpha and beta forms of LGA on the materials flow, consolidation, and tableability. This study also aims to provide a proof of concept platform for the further application of XCT methods to the study pharmaceutical materials processing and formation.

2. EXPERIMENTAL METHODOLOGY

2.1. Chemicals and Preparation. L-Glutamic acid $\text{C}_5\text{H}_9\text{NO}_4$, molecular weight: 147.13, Reagent Plus $\geq 99\%$ was used as supplied by Sigma-Aldrich. Deionized water was used for recrystallization studies. L-Glutamic acid was recrystallized to prepare the two polymorphic forms, alpha and beta, using a HEL Autolab 0.5 L jacketed vessel with temperature control provided through a Julabo F32 with attached PT100 thermocouple which was inserted into the reactor. The contents of the vessel were agitated by constant stirring at 200 rpm using a three blade pitched impeller. To recrystallize the metastable alpha form, a solution of L-glutamic acid in deionized water at 30 g/kg concentration was prepared in the reactor. This was then subjected to a heating cycle from 25 °C to a holding temperature of 90 °C for 1 h to allow full dissolution of solids. The solution was then cooled at 0.7 °C/min to a lower holding temperature of 5 °C, where the recrystallized solids were isolated using vacuum filtration and dried in an oven at 40 °C. To obtain the beta form solids, the methodology used for the alpha form was repeated; however, the solution concentration was increased to 50 g/kg, and the cooling rate was decreased to 0.1 °C/min.

2.2. Scanning Electron Microscopy (SEM). The samples were prepared for scanning electron microscopy by dispersing 1 mg of the powder from each specimen onto adhesive Sticky Tabs placed on 12.5 mm diameter aluminum pin stubs. An amount of excess powder was removed by tapping the stubs, and the prepared specimen stubs were sputter coated with a thin (approximately 10 nm) deposit of platinum using a Quorum Q150TS coating unit operated at 20 mA for 1 min using argon gas. The specimens were examined using a Carl Zeiss SMT SUPRA 40VP field emission scanning electron microscope (FE-SEM). The FE-SEM was operated at high vacuum with an accelerating voltage of 3 V, and a specimen working distance of 12 mm. Secondary electron images were recorded at magnifications of 50 \times and 200 \times .

2.3. Bulk and Tapped Density Measurement. The tap density apparatus (model SVM10, Copley/Erweka, Nottingham, UK; lift height 3 mm, tapping frequency 150 taps/min) was used to determine bulk and tapped density and Carr's compressibility index. A tared 250 mL measuring cylinder was filled with test material to 100 mL, and the volume and weight of the material were recorded. With minimal disturbance to the measuring cylinder, it was transferred to the tap density apparatus. From the volume and recorded mass, the bulk and tapped density were calculated.

2.4. Tableting Studies of L-Glutamic Acid Powders. The tableting test was performed using a Gamlen Tablet Press (GTP-1, Gamlen Tableting Limited, Nottingham, UK). A total of 100 mg of sample was compacted in a 6 mm die at a compaction pressure of 180 MPa and a speed of 60 mm/min. Prior to tablet ejection, the detachment stress of the base die was measured manually using a 50 kg hand-held force gauge (Mecmesin, Slinfold, UK) placed at the side of the base die.

2.5. X-ray Computed Tomography (XCT). **2.5.1. Data Acquisition.** Sample mounts for the two powders were created by gluing a 2 cm length of 3 mm diameter polyamide tubing to a nail (see Figure 1a). Alpha (mean size 200 μm) and beta (mean size 250 μm) glutamic acid was poured into a sample mount to half of the height, and an initial low-resolution scan was conducted in a Zeiss Xradia 520-DCT Versa system. The voltage was 80 kV, and the power was 7 W; a 4 \times objective magnification lens was used, with source and detector distances of 31.02 mm and 8.00 mm respectively giving a voxel size of 5.37 μm^3 . A 2 \times detector binning was used, and 1601 projections were collected with a 0.5 s exposure time. The sample mount was removed from the Versa system and tapped by hand 10 times, before scanning again with the same scan parameters. This process was repeated giving scans after 0, 10, 20, and 30 taps. Finally, high resolution scans were performed. The voltage and power were the same as for the low-resolution scans, but 1 \times detector binning, 10 \times objective lens, and source and detector distances of 10.01 mm and 23.71 mm gave a voxel size of 1.00 μm^3 . A total of 3201 projections were collected with a 4 s exposure time. A sample of beta glutamic

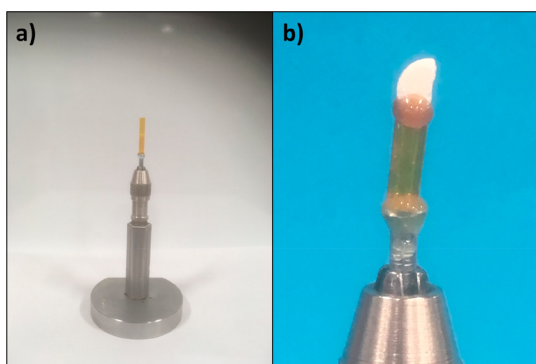


Figure 1. Sample arrangements for the X-ray computed tomography experiments (a) a sample of alpha glutamic acid powder free flowed into a polyamide tube, (b) half tableted sample of the alpha glutamic acid was mounted by using a polyamide tubing fixed to a nail using epoxy resin; for reference, the Kapton tube is 3 mm in diameter, and the nail is 2.3 mm in diameter.

acid was similarly created, and the same scanning procedure was followed. Because of a limited amount of instrument beamtime available, only two repeats of the tapping experiment for alpha were possible and only one experiment for beta. Results for both alpha experiments have been provided in S1 and S2 of the [Supporting Information](#). A portion of a tablet of alpha glutamic acid, created from crystals larger than $200\ \mu\text{m}$ compressed with 180 MPa, was fixed to the end of Kapton tubing using epoxy (see [Figure 1b](#)). This was scanned at 40 kV and 3 W using a 1 \times detector binning, source and detector distances of 16.04 mm and 8 mm respectively and a 4 \times objective lens. A total of 3201 projections were collected with 10 s exposure times. The resulting voxel size of the reconstructed volume was $2.25\ \mu\text{m}$. A small portion of the breakage interface was also scanned at a higher resolution, using the 10 \times objective lens, 1 \times detector binning and a pixel size of $0.78\ \mu\text{m}$. For this scan, the voltage was 65 kV, the power was 5.5 W, and the source and detector distances were 12 mm and 9 mm. A total of 3201 projections were collected with an exposure time of 7 s.

2.5.2. Data Analysis. All of the data sets were reconstructed with the native Zeiss Reconstruction software using the FDK algorithm to form 3D virtual volumes of the samples, as shown in [Figure 2a](#). The 3D virtual volume is essentially a 3D matrix that discretizes the sample into individual voxels, with each element of the matrix having a greyscale value that is proportional to the atomic weight of the material within the corresponding voxel of the sample. These 3D volumes were loaded into the commercial software Avizo (Thermo Fisher Scientific, USA), with the low-resolution scans filtered using a nonlocal means algorithm. A virtual horizontal slice through the filtered data is shown in [Figure 2b](#), showing distinct greyscale values between the air (dark) and the tube and LGA particles (light). A mask of the analysis region ([Figure 2c](#)) was created with the analysis performed above the glue level to avoid local surface effects of the glue on the powder bed. The powder was segmented using autointensity partitioning, with [Figure 2d](#) showing the identified particles. For each slice, the volume fraction was calculated as the ratio of powder volume to analysis volume region. In other words, the volume fraction is the ratio of red area in [Figure 2d](#) to red area in [Figure 2c](#). The powder density was calculated from the volume fraction by multiplying by the material density. As the powder densifies, there is a higher proportion of particles per unit volume, and so a higher proportion of voxels shows as a lighter gray color. This gives a higher volume fraction and thus a higher tapped density. Horizontal slices, one voxel apart along the axial coordinate of the powder bed, were analyzed to calculate the density at that bed height. A total of 758 slices were used for alpha and 828 slices for beta, with the difference between the polymorphs due to differing amounts of glue in the final volume.

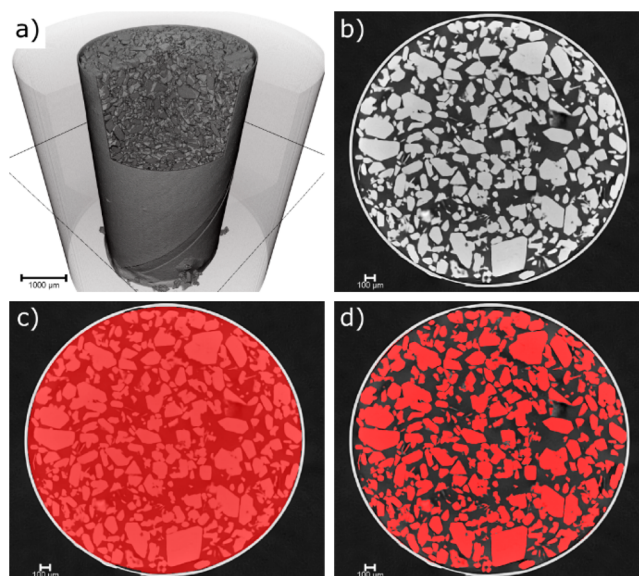


Figure 2. (a) A 3D visualization of the low-resolution scan of the bed after 30 taps, with a small section cutaway revealing the powder inside. (b) A horizontal virtual slice through the powder bed, perpendicular to the axial coordinate, after filtering with a nonlocal means filter. (c) The same slice overlaid with the analysis mask. (d) The same slice overlaid with particles identified within the analysis mask.

The data were smoothed using a sliding mean with a window of 100 slice measurements. This corresponds to a physical window length of $537\ \mu\text{m}$, which is more than 2 \times the average particle size and hence effectively allows the main pattern in the tap density as a function of bed height to be seen without local variations due to either differently sized individual particles or due to the position of virtual slicing of the bed. The entire volume of the analysis region and the entire volume of particles contained within that region were used to calculate the overall bulk and tapped densities. As the volume of the analysis region remains constant between tapping, the Carr's index, C , was calculated using eq 1,

$$C = 100 \frac{\rho_T - \rho_B}{\rho_T} \quad (1)$$

where ρ_T is the tapped powder density and ρ_B is the bulk density of a free flowed powder.

Individual particles were identified using a watershed and morphological edge operation approach,¹⁹ with the inclination of the maximum Feret diameter (hereafter called the Feret length) used to measure the orientation of the particles for each run. The detail provided by the high-resolution scans was used to qualitatively examine the crystallographic orientations in the final tapped state.

3. RESULTS

3.1. Crystal Morphology of the Alpha and beta Form.

The morphology of the recrystallized L-glutamic acid polymorphs, alpha and beta, are provided in [Figure 3](#), panels a and b, respectively. The SEM images highlight that the external habit of the alpha polymorph is prismatic being dominated by the large $\{0\ 0\ 2\}$ top surfaces and side $\{1\ 1\ 1\}$ surfaces. Conversely, the beta polymorph crystallizes as needle-like crystals which are also dominated by large slow growing $\{0\ 0\ 2\}$ top surfaces. The alpha crystals were found to largely remain intact following filtration with a low amount of breakage, exhibiting well-defined crystallographic surfaces; the beta crystals were found to exhibit large degrees of breakage

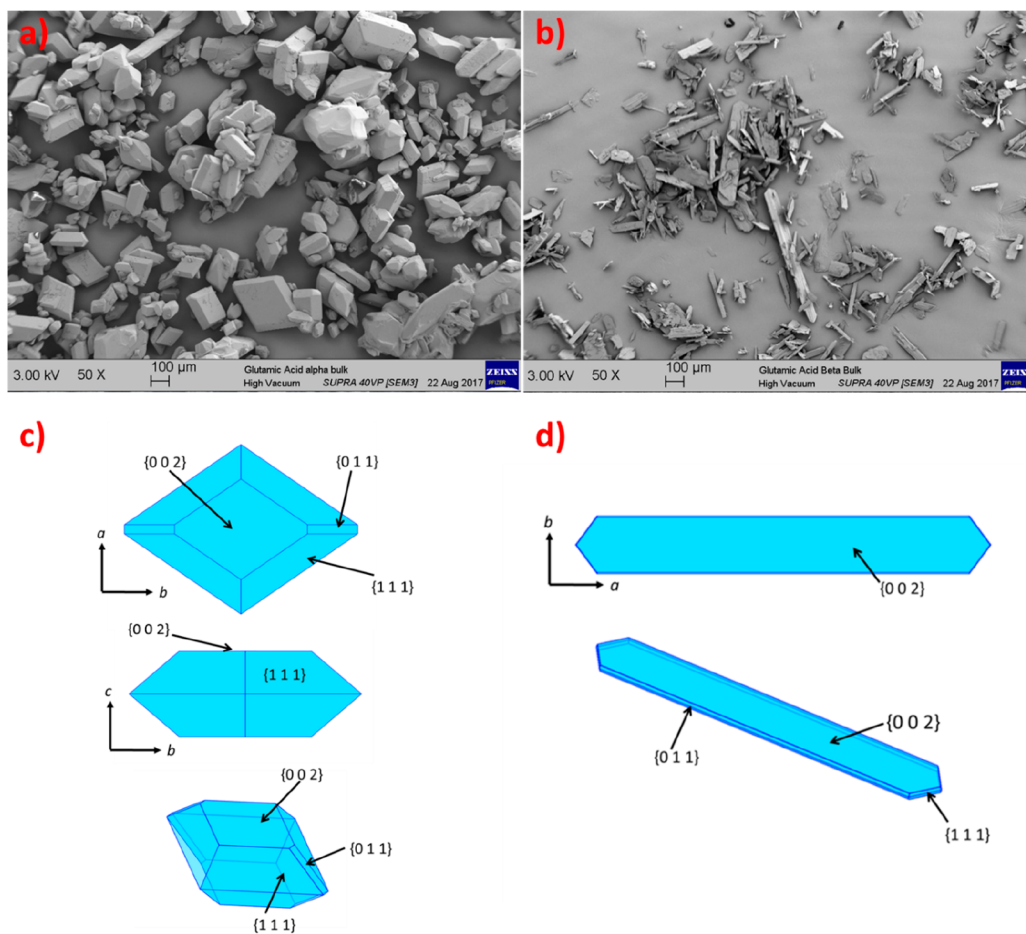


Figure 3. (a) SEM image of alpha crystals grown from water solutions highlighting their prismatic morphology, (b) SEM image of beta crystals grown from water solutions showing their needle-like morphology, (c) alpha and (d) beta form of LGA simulated morphology showing α -form crystallizes in a prismatic morphology, while the stable β -form crystallizes with a needle-like morphology.

following filtration and were less well-defined crystallographically.

3.2. Studies of Powder Packing of Alpha and Beta Polymorphs. Figure 4 provides example virtual vertical cross-sectional slices viewed perpendicular to the axial coordinate of the alpha and beta powder beds during consolidation

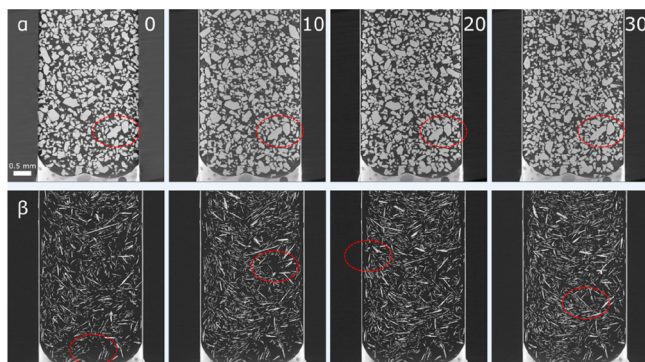


Figure 4. 2D reconstructed slices from the XCT scans viewed perpendicular to the axial coordinate for the packed columns of alpha (top, run 1) and beta (bottom) powders; the sequence highlights the influence of tapping (number of taps inset in the image) on the consolidation of the powder beds, going from a free flowed powder (far left) to the powder bed after 30 taps (far right).

experiments using the reported column tapping methodology. An initial qualitative analysis of the powder bed morphology of the two polymorphs reveals some striking differences between the two: the first is the obvious increased densification of the alpha powder bed during the consolidation process when compared to the beta powder bed. This is particularly evident by the number of particles which fail to reorganize their spatial or angular position within the alpha bed structure, an example of which is highlighted by the particles in the red circles on the top row of Figure 4. Analysis of the vertical inclination angle of the ferret length, shown in S3 of the Supporting Information, confirms that there is no change in the vertical orientation of the particles. This suggests that the alpha form reaches its optimum packing efficiency at a higher rate compared to the beta material. Second, the large amount of void space present within the beta packed bed when compared to the alpha packed bed was evident from analysis of the reconstructed images of the packed columns in Figure 4. The void spaces in the beta structure appeared at various locations within the columns and seemed to be caused by poor geometrical orientation of the beta particles; this is highlighted in the red circles in the lower sequence of images in Figure 4.

Further analysis of the reconstructed XCT images shown in Figure 4 yielded the volume of the powder together with the void spaces in the powder beds and thus allows a quantitative analysis of the bed density as a function of consolidation. The

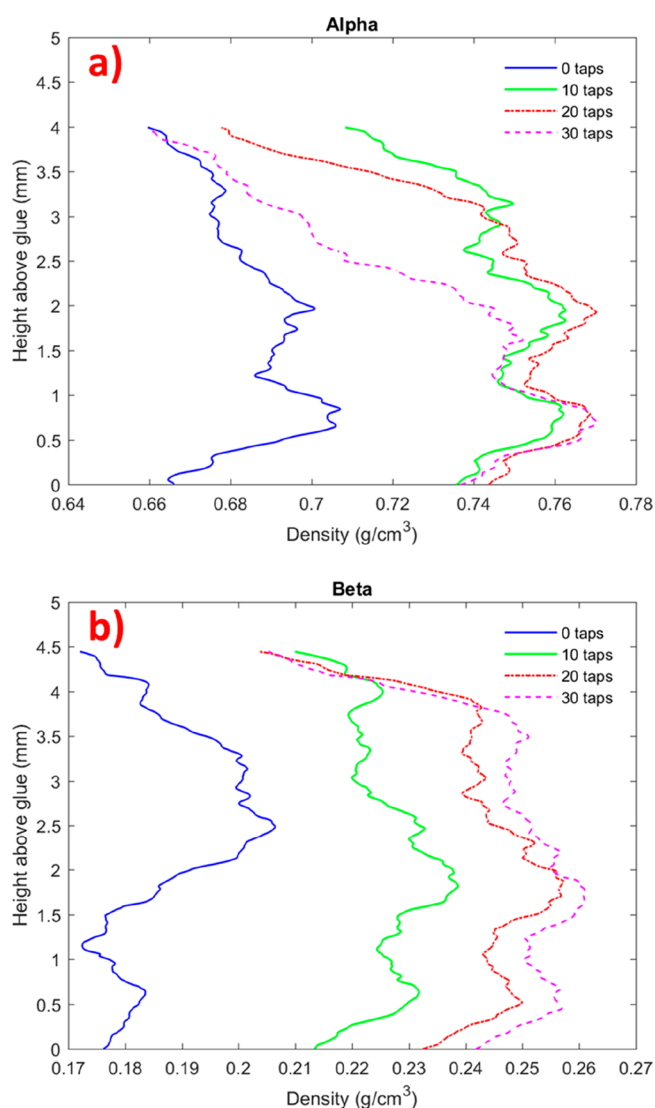
Table 1. Measured Bulk Density, Tapped Density (g/cm^3) Carr's Index and Hausner's Ratio of Alpha and Beta LGA through Both Conventional "Tapping Down" Commonly Used in Industrial Practice and the Current XCT Experiments

polymorphic form	measured powder density by the "tapping down" method	measured powder density by XCT method (number of taps)				
		0	10	20	30	
alpha	bulk density (g/cm^3)	0.632				
	tapped density (g/cm^3)	0.788	0.684	0.746	0.746	0.724
	Carr's index	19.7		8.2	8.2	5.5
	Hausner's ratio	1.25		1.0893	1.0895	1.0583
beta	bulk density (g/cm^3)	0.217				
	tapped density (g/cm^3)	0.335	0.187	0.226	0.243	0.248
	Carr's index	35.2		17.1	22.8	24.4
	Hausner's ratio	1.54		1.2058	1.2953	1.3225

bulk and tapped densities for the two powders calculated from the tomographic images together with data from a conventional "tapping down" method are compared in Table 1. The bulk and tapped powder densities through the "tapping down" method for the alpha form were measured as $0.632 \text{ g}/\text{cm}^3$ and $0.788 \text{ g}/\text{cm}^3$ respectively and $0.217 \text{ g}/\text{cm}^3$ and $0.335 \text{ g}/\text{cm}^3$ respectively for the beta form. This yields a Carr's index of 19.7 and 35.2 for the alpha and beta forms respectively; this index is typically used in many industries to assess the flowability of powders. A value of 19.7 would be classified as fair flowability, and a value of 35.2 would be classified as very poor flowability.³⁷

Exploiting the data from tomographic imaging, the initial bulk densities of the alpha (run 1) and beta powders were calculated to be $0.684 \text{ g}/\text{cm}^3$ and $0.187 \text{ g}/\text{cm}^3$ respectively. These values were comparable to those measured through the conventional "tapping down" method. Upon consolidation of the alpha powder bed, there was an initial sharp increase in powder bed density to a value of $0.746 \text{ g}/\text{cm}^3$ after 10 taps, followed by a stable value of $0.746 \text{ g}/\text{cm}^3$ after 20 taps and slight decrease to $0.724 \text{ g}/\text{cm}^3$ after 30 taps. The beta form powder bed was found to also undergo a sharp increase in bed density during the initial consolidation phase to $0.226 \text{ g}/\text{cm}^3$; however, conversely to the alpha bed structure, there is a steady increase in powder bed density during the experiments from 0.243 to $0.248 \text{ g}/\text{cm}^3$ after 20 and 30 taps, respectively. This analysis reveals that the alpha powder reaches its optimum packing density of $\sim 0.75 \text{ g}/\text{cm}^3$ much faster than the beta phase, which appears to be still undergoing rearrangement and bed densification following 30 taps. Overall the values of the powder bed densities measured through XCT methods agree well with those measured through the "tapping down" method, particularly for the alpha form, whereas for the beta form, it is probable that the bed did not reach a steady state of densification and hence the larger difference of the tapped densities measured by the two methods.

Analysis of the XCT data allowed the density variations as a function of bed height to be revealed. The smoothed data are plotted in Figure 5a,b for the alpha (run 1) and beta powder beds respectively as a function of the number of taps (consolidation) during the experiment. Figure 5a reveals that the alpha bed structure contains a high-density region at the bottom of the bed $\sim 1 \text{ mm}$ above the tube base; this region undergoes a significant increase in densification between 0–10 taps during the initial consolidation phase. The high-density region then undergoes a more gradual densification between 10 taps and 30 taps. This is most likely due to rearrangement of the particle bed where the larger particles segregate toward

**Figure 5.** Variation in powder bed density of (a) alpha (run 1) and (b) beta LGA along the powder bed axial coordinate, where the higher the height in mm the closer to the top of the bed, as a function of the number of taps (T1 = 0 taps, T2 = 10 taps, T3 = 20 taps, T4 = 30 taps).

the bottom of base of the bed, and the smaller particles fill the voids between these larger particles. Conversely, the top of the alpha bed structure undergoes an initial densification followed by a rapid loss of bed density between 10 taps and 30 taps,

which is likely to be due to the overall segregation of the particles and subsequent reduction in bed height.

The Supporting Information, S1 and S2, contains a comparison between the two experimental runs for alpha. Although run 2 shows slightly different behavior, with a densification after each set of 10 taps, there is less than 5% difference in the tapped densities at each stage. This is encouraging considering that there was likely to be differences in the strength of the taps between each scan as the tapping was performed by hand. There would also be differences arising from the initial filling of the powder bed and from the construction of the sample mount. The strength of the tapping could also be the reason for the decrease in the tapped density between 20 and 30 taps in run 1. Close examination of the tapped density against height for run 1 shows that there is densification in the bottom 1 mm, with the bed becoming less dense above this height. Observations showed that the top of the powder bed, from 5 mm to the surface at 10 mm, was prone to fluidization, hence why the lower portion of the bed closest to the glue was always scanned in XCT. In this particular case, i.e., 30 taps in run 1, the nature of the tapping may have caused a larger proportion of the bed to be fluidized.

Figure 5b highlights how the powder bed structure of the beta form behaves very differently to that of the alpha form during the consolidation process. The densification of the bed is a more gradual process and following the initial densification during 0–10 taps, the shape of the density profile is then very homogeneous from 10 taps to 30 taps in comparison to the alpha bed structure. This is most likely caused by the needle-like particle morphology of the beta phase restricting the geometrical reorientation of the particles within the bed resulting in a more isotropic densification process, where the variation in density in the axial coordinate of the bed varies to a lesser extent than in the case of the alpha bed structure. Critically, this analysis highlights the fundamental differences in the consolidation process of the alpha and beta packed beds, where the prismatic morphology of the alpha form allows significant reorientation of the particles within the powder bed leading to very high-density regimes at the bottom of the column. In contrast, the beta phase morphology restricts particle reorientation, and hence its consolidation is more isotropic throughout the axial coordinate of the bed, where the overall bed morphology changes very little in comparison to the case of alpha.

The impact of the particle morphology on the consolidation process is further highlighted in Figure 6, which shows a high definition 3D cross sectional image through the powder beds of alpha (a) and beta (b). The alpha bed morphology is shown to consist of the large prismatic particles orientated in such a manner that the $\{0\ 0\ 2\}$ surfaces point vertically upward; i.e., the normal to the surface lies parallel to the axial coordinate of the powder bed. Note that the previous geometric analysis using the Feret length is not sufficient for checking the orientation of the $\{0\ 0\ 2\}$ face. Consider the middle picture in Figure 3c. Here the Feret length is orientated horizontally with the $\{0\ 0\ 2\}$ face pointing vertically upward. However, if the particle was rotated by 90° about the b axis, the Feret length would still be horizontal, but now $\{0\ 0\ 2\}$ would also be horizontal. Nevertheless, careful analysis of Figure 6 bearing in mind the morphology of Figure 3c shows the $\{0\ 0\ 2\}$ face to be pointing vertically upward, increasing the packing efficiency. Additionally, it was found that the smaller particles arranged within the gaps between the larger crystallites and that their

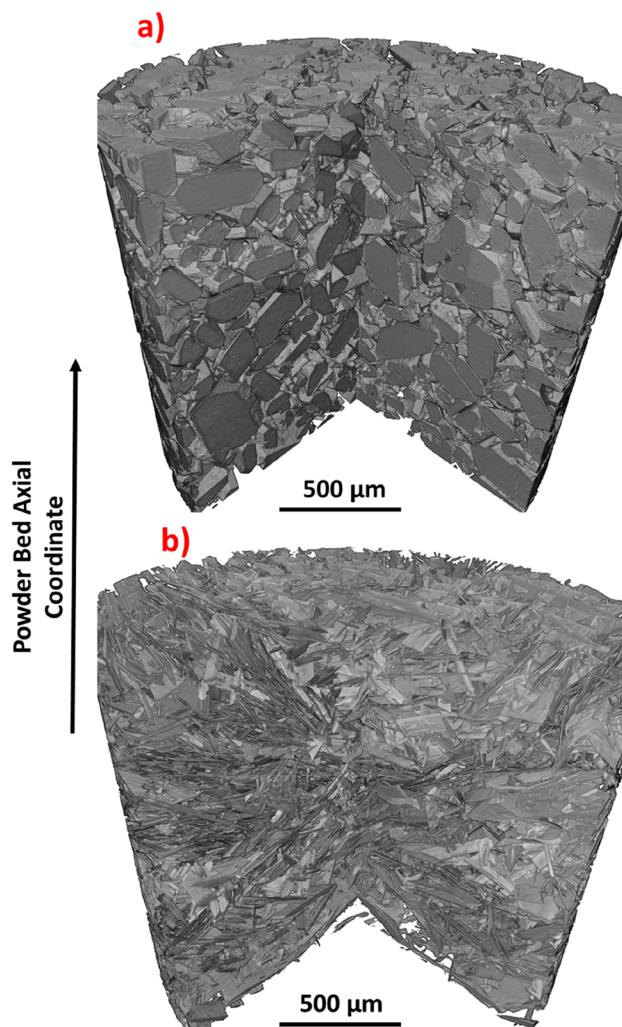


Figure 6. Reconstructed image cross-section of the powder beds from XCT analysis of (a) alpha and (b) beta powders, the 3D image provides a view of the powder bed morphology and its variation along the axial coordinate.

relative orientation was more random with respect to the bed axial coordinate. In contrast, the beta bed structure, shown in Figure 6b, consists of the needle particles assembled into a “web” like structure due to preferred orientation of the particles needle axis perpendicular to axial bed coordinate. This appears to cause “tangling” of the particles where large amounts of void space is observed between particles resulting in the lower measured density of the bed in relation to the alpha bed morphology.

3.3. Evidence for the Initiation of Polymorphic Transformation from the Metastable Alpha Form to the Stable Beta Form. Detailed examination of the high resolution XCT scans of the alpha phase powder also revealed the presence of a few crystallites of the stable beta phase in close proximity to the alpha crystals as shown in Figure 7. The alpha phase is known to be metastable relative to the beta phase and can undergo a monotropic phase transformation to the stable beta structure in the presence of moisture. Previous work^{38–40} has shown that this polymorphic transition can proceed through the secondary nucleation of the beta phase on the $\{0\ 1\ 1\}$ and $\{1\ 1\ 1\}$ habit faces of the alpha crystals, where the fast growing $\{1\ 0\ 1\}$ needle capping surfaces of beta form

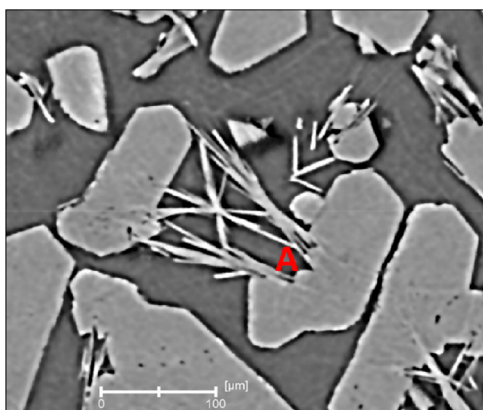


Figure 7. A virtual vertical cross-section through the high-resolution XCT scan of the final alpha powder bed showing the existence of needle-like beta crystals following polymorphic transformation.

can be nucleated by the template provided by the availability of free (unbound) amino groups at the transformation interface. This mechanism, whereby the needle-like beta crystals seem to have nucleated on the alpha crystals, can be seen in [Figure 7](#). Although it is difficult from this analysis to fully assess the initial nucleation point of the beta phase, the images do show an interesting interaction between the two polymorphic phases. The beta crystals at point A in [Figure 7](#) seem to be “consuming” the alpha phase as they have nucleated and begun to grow not only from but also into the $\{0\ 0\ 2\}$ surface of a nearby alpha crystal. Interestingly, examination of the initial alpha phase powder by powder X-ray diffraction (PXRD) found no evidence for the presence of the beta phase. Mindful that previous work has shown that PXRD can only routinely measure polymorph content to a lower limit of ca. 0.5 wt %, ⁴¹ this would suggest that the quantity of the beta phase present within the alpha form powder would be likely to be significantly less than this, highlighting, in turn, the sensitivity of the XCT method. Although not a major focus of this paper, this observation demonstrates the potential utility of XCT in studying polymorphic interconversion at its early stages, for example, during powder storage and subsequent processing, and that this could be a motivation for more detailed studies in the future.

3.4. Structural Analysis of Tablet Consolidation. To further explore the consolidation behavior of the L-glutamic acid polymorphs, pure powders were compacted into tablets where the alpha form produced tablets of medium tensile strength, and the beta form could not be compacted into tablets of any tensile strength at the same compaction pressures; examples are provided in [Figure 8](#).

To investigate the observed compaction differences between the two polymorphic forms the internal structure of the alpha tablet was investigated, and a 3D reconstruction of the compact is provided in [Figure 9](#), which highlights vertical and horizontal cross sections through the tablet. An initial qualitative analysis of the 3D reconstruction reveals that there are different density regions within the tablet. The first are high-density regions shown in white in the cross sectional images, and the second are low-density regions shown in gray, together with pockets of trapped air, which are revealed in black in the images. Interestingly, the higher density regions appear to be single crystals of alpha, which survive the high pressure compaction process, and the lower density regions

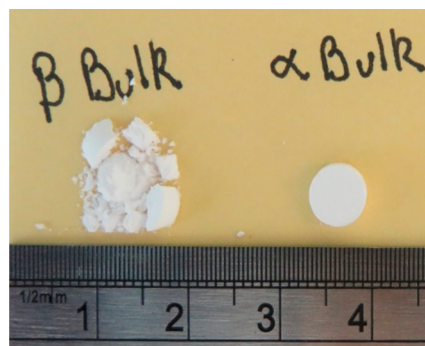


Figure 8. Image of example compacts of the alpha and beta powders once compacted on a Gamlen tablet press, the alpha powder (right) compacts to well-formed tablets of intermediate tensile strength, whereas the beta powder (left) forms compacts of zero tensile strength.

appear to be particles that have undergone significant size reduction to a fine powder. In general, the fine powder in the low-density regimes links the higher density particles by filling the void spaces between them. These high-resolution images also show fine microcracks within the single alpha crystals where the majority originate at the $\{0\ 0\ 2\}$ surface and run perpendicular to the face normal.

A histogram of the entire image is provided in [Figure 10](#) to give a quantitative assessment of the tablets' internal structure. This indicates that there are two very distinctive density regions inside the tablet which can be separated based on their pixel grayscale value. The data in [Table 2](#) show that 2% of the tablet is void space of trapped air, and 98% is L-glutamic acid and the high-density regions make up 44.2% of the tablet and 53.8% is made up of the low-density regions. It should be noted that to differentiate between the high- and low-density regimes within the tablet, the X-ray tube voltage was set to a low value, and hence the images had a lower resolution of $\sim 2.25\ \mu\text{m}$. This lower resolution increased the difficulty in separating the solid/air interface during the analysis and would explain the particularly high values of solid present within the compact measured in this experiment.

This analysis demonstrates that large regions of the compact comprise large dense alpha crystallites which do not appear to disintegrate on compaction, and in contrast, large regions exist where the powder has undergone a dramatic size reduction to a fine powder. This is surprising since the initial alpha powder which was filled into the die was shown to have a reasonably large size distribution of 100–200 μm as shown in the SEM images in [Figure 3](#), and yet more than half of the tablet mass is made up of a very fine powder. This leads to a hypothesis that the smaller particles within the alpha powder distribution are reduced to a very small size $\sim <10\ \mu\text{m}$, but the larger particles withstand the compaction pressures and are distributed throughout the compact within the finer powder. Further studies as a function of compaction force are required to quantify this.

To further investigate the fracture mechanism of the observed cracked intact alpha particles, individual crystallites were isolated from the 3D reconstruction shown in [Figure 9](#), and their microstructure were investigated. [Figure 11](#) shows two particles and their location within the tablet on the left of the image (a and c) and a semitransparent rendering of the same particles with the trapped air between fracture surfaces highlighted in green, on the right (b and d). The internal

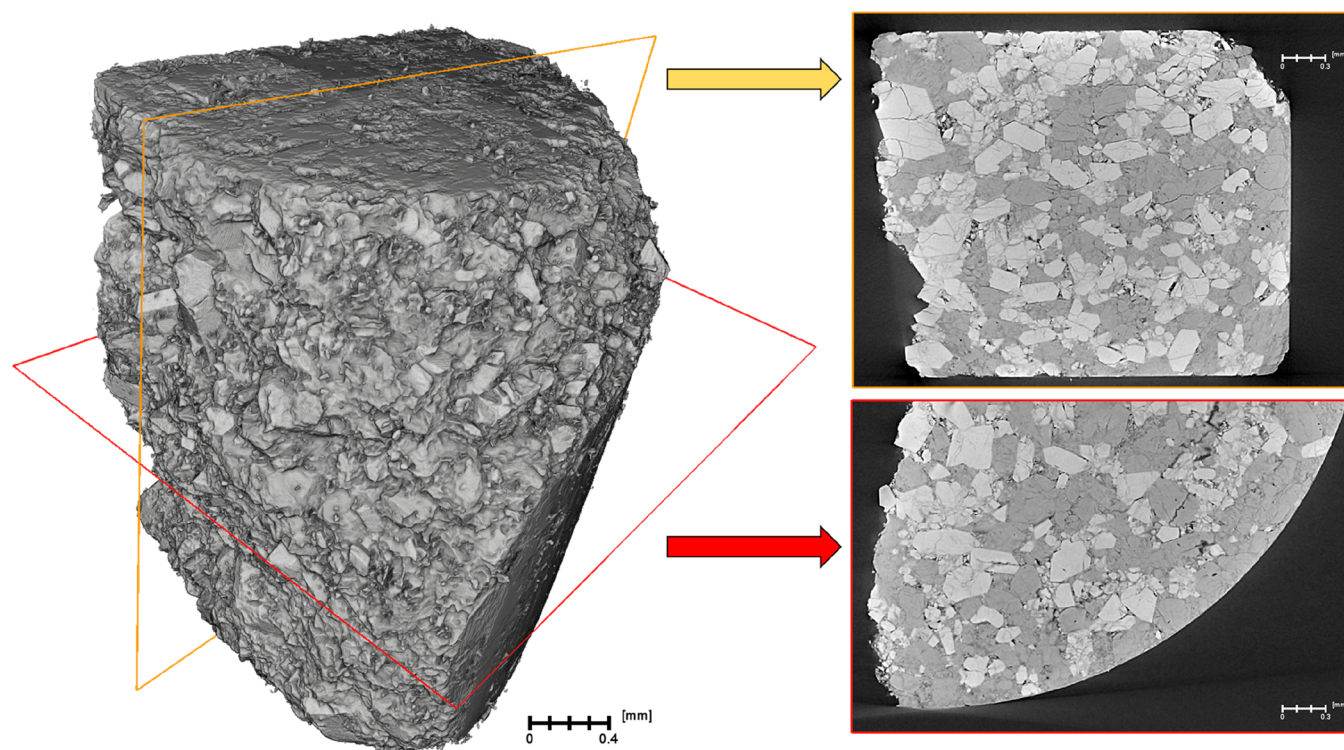


Figure 9. Vertical and horizontal cross-sections (right) through the X-ray reconstructed volume (left) of the alpha form tablet, highlighting the different powder density regions and the intact single particles of alpha LGA.

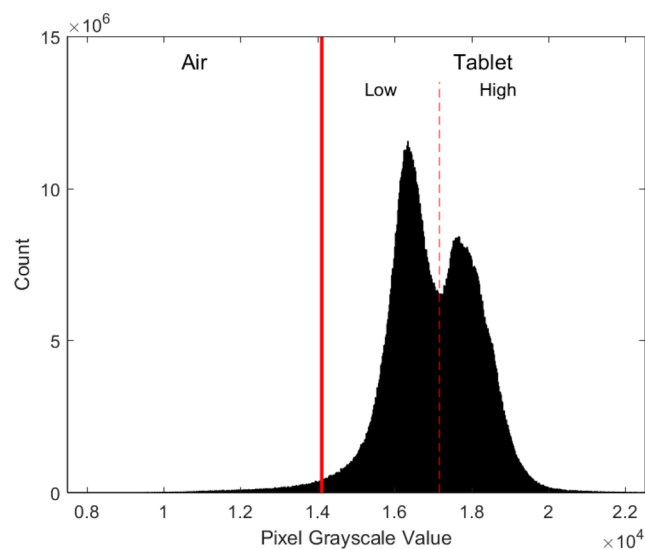


Figure 10. A histogram of the entire image highlights two areas of significantly different densities within the alpha tablet.

Table 2. Analysis of the Volume Fraction within the Alpha Tablet, with Calculations Highlighting the Amount of High versus Low Density Material by Their Respective Volumes within the Tablet

% air (within tablet)	2.0
% solids (within tablet)	98.0
% low density	53.8
% high density	44.2

cracks within the particles can be seen where the mechanism of fracture is confirmed to start perpendicular to the $\{0\ 0\ 2\}$

surfaces, and this is the case for both cracks in both crystallites. Close examination of the powder grain microstructure did not reveal the obvious existence of any substantial plastic deformation, which might be evidenced by particles containing bands of slip planes. Examination of the 3D packing for LGA (see Figure 12) suggests that the most likely fracture surface would be $\{0\ 0\ 2\}$. The intact crystals were found to be orientated with respect to the compaction force normal to this plane, hence with no resolved shear stress along the preferred fracture plane, and then fracture along the $\{0\ 0\ 2\}$ planes would not be feasible. This perhaps explains why fracture surfaces observed were through secondary fracture planes, notably, $\{1\ 1\ 0\}$ and $\{1\ 0\ 1\}$.

4. DISCUSSION AND CONCLUSIONS

This work demonstrates a novel application of modern X-ray computed tomography techniques to study the fundamental consolidation properties of the related alpha and beta polymorphic phases of L-glutamic acid. The alpha form was found to consolidate under gravity much more effectively than the beta form in powder tapping experiments, where the alpha form taps down to a final value of 0.724 g/cm^3 compared to value of 0.248 g/cm^3 for the beta phase. Qualitative assessment of high resolution XCT scans suggested that this caused by the alpha morphology, which stacks perpendicular to its $\{0\ 0\ 2\}$ surface and where smaller particles fill the remaining voids. Conversely, the beta form stacks with its needle axis broadly perpendicular to the powder bed axial coordinate forming a “web” of interlocked particles which reduces the bed’s ability to reorientate the particles. XCT imaging of an alpha tablet revealed two distinct density regimes within the tablet where high-density regimes were made up of single crystals and the low-density regimes of fine powder.

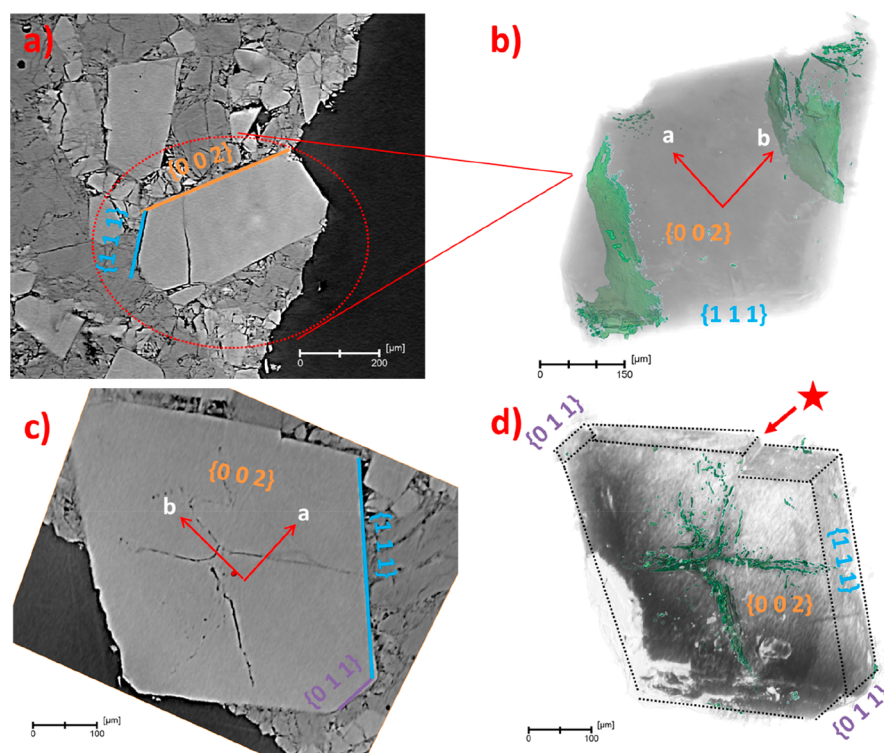


Figure 11. Visualization of two separate single particles, (b) and (d) from the breakage interface of the alpha tablet (a) and (c) respectively where particle (b) has been reoriented relative to the image in (a) to show clearly the cracks within the crystal. These reconstructions highlight the characteristic $\{0\ 0\ 2\}$, $\{1\ 1\ 1\}$, and $\{0\ 1\ 1\}$ surfaces of the alpha morphology. The crystallographic axes have been provided with red arrows to show the orientation of the a and b axes. The particles have been rendered transparent to expose the microstructure within, revealing the fracture planes of the particles to be perpendicular to the $\{0\ 0\ 2\}$ surfaces, and the regions shown in green indicate areas of air trapped between two fracture surfaces. The crystal in (d) also shows characteristic slip (more obvious at surface with * red arrow) of the plane parallel to the crack shown in green.

The analysis of both the powder bed and tablet would be enhanced further through validation of the crystal orientations. The geometric orientations used earlier in this work could not distinguish between different crystallographic planes, and hence other methods are needed to validate the qualitative assessments. However, traditional methods such as wide-angle X-ray scattering (WAXS) would require the sample to be modified from the XCT preparation making a direct comparison and validation impossible. Laboratory Diffraction Contrast Tomography (LabDCT) has recently emerged as a laboratory technique for measuring crystal orientations of metals, metalloids, and silicon, with work currently underway to extend this to organic polycrystalline solids.⁴² Proof of concept work has been carried out using synchrotron radiation on the case study system L-glutamic acid, and the hope is this will be extended to laboratory sources for organic crystalline materials.⁴³ This would provide a natural way to enhance the XCT results with crystallographic information.

These findings demonstrate the utility of the current state of the art XCT capabilities to identify the morphology of individual particles together with interparticle microstructure, notably, density distributions, in practical organic processing systems. This study has also provided some critical 3D powder processing data which can be used to improve computational simulations of such behavior using finite and discrete element methods (FEM and DEM) of powder flow, consolidation, and compaction to simulate how changes in the solid form have the potential to impact during processing.^{44,45} In particular, the use of voxel-based DEM simulations^{46–48} has the potential to

embed crystal surface-specific parameters into the simulations to predict the behavior of faceted particulates as a function of processing, and through the provision of XCT data much more representative DEM models may evolve in time.

This work was an initial proof of concept study, and while results are encouraging, further work is needed to understand the precision of the XCT experiments. Repeated measurements using the same exact setup would allow the experimental error to be quantified. Standardization of the sample mount, initial filling, and tapping would also increase the precision of the technique, but would require methods to be developed for repeatedly loading the tube and an automated tapping mechanism synchronized with the XCT equipment.⁴⁹

This proof of concept work also has the potential for characterizing the behavior of formulated pharmaceutical systems, e.g., the impact of varied concentrations of active pharmaceutical ingredients and excipients within a formulation on processing performance, potentially leading to the development of simulation tools and workflows for optimizing, e.g., the content uniformity of formulations in terms of their blending, flow, and compaction unit operations. The latter is particularly timely regarding current interest in the multiscale design of continuous direct compression manufacturing processes.^{50,51} Such studies may also benefit from combining laboratory-based XCT for quasistatic analysis coupled with the use of synchrotron radiation based tomographic imaging to study the dynamics of particle processing under representative conditions.

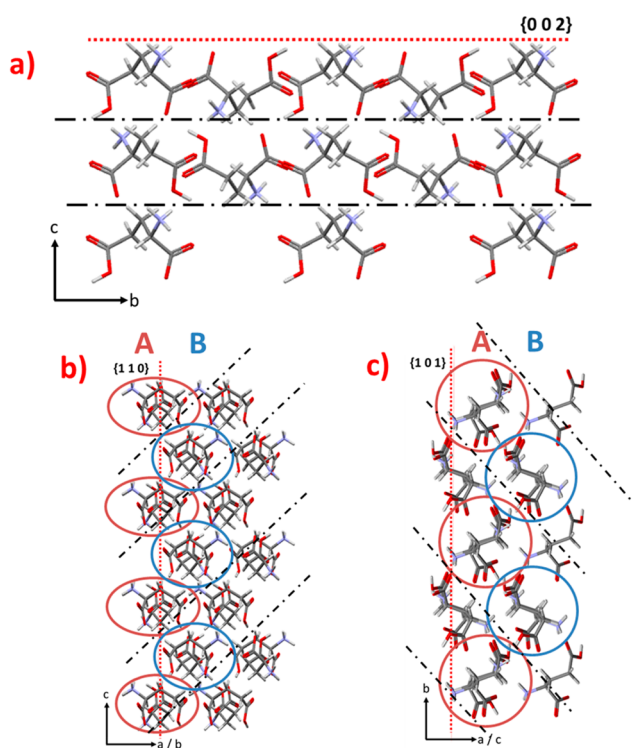


Figure 12. Crystallographic packing diagrams of the alpha structure highlighting (a) the $\{0\ 0\ 2\}$ surface (red line) viewed down the a axis to highlight the possible $\{0\ 0\ 1\}$ fracture plane (black lines), (b) the possible secondary $\{1\ 1\ 0\}$, and (c) $\{1\ 1\ 0\}$ fracture planes viewed perpendicular to the plane, the molecules circled in red and blue labeled A and B indicate the two layers which may slide over one another in a direction in the plane.

In short, the proof of concept data and analysis in this manuscript show how XCT could provide invaluable information as to how particulate surfaces interact within 3D powders, providing new leads for investigating the surface chemistry origins of the interparticulate interactions.

■ ASSOCIATED CONTENT

Supporting Information

The Supporting Information is available free of charge at <https://pubs.acs.org/doi/10.1021/acs.cgd.9b01515>.

Bulk and tapped density measurements, the powder bed density variation with bed height through tomography analysis, and the calculated ferret length inclination of the alpha crystals from tomographic analysis (PDF)

■ AUTHOR INFORMATION

Corresponding Author

T. D. Turner – Centre for the Digital Design of Drug Products, School of Chemical and Process Engineering, University of Leeds, Leeds LS2 9JT, U.K.; orcid.org/0000-0003-3776-2044; Email: t.d.turner@leeds.ac.uk

Authors

P. Gajjar – Henry Royce Institute, Department of Materials, School of Natural Sciences, University of Manchester, Manchester M13 9PL, U.K.

I. S. Fragkopoulos – Centre for the Digital Design of Drug Products, School of Chemical and Process Engineering, University of Leeds, Leeds LS2 9JT, U.K.

J. Carr – Henry Royce Institute, Department of Materials, School of Natural Sciences, University of Manchester, Manchester M13 9PL, U.K.

T. T. H. Nguyen – Centre for the Digital Design of Drug Products, School of Chemical and Process Engineering, University of Leeds, Leeds LS2 9JT, U.K.; orcid.org/0000-0002-6752-1455

D. Hooper – Pfizer Worldwide Research and Development, Sandwich CT13 9NJ, U.K.

F. Clarke – Pfizer Worldwide Research and Development, Sandwich CT13 9NJ, U.K.

N. Dawson – Pfizer Worldwide Research and Development, Sandwich CT13 9NJ, U.K.

P. J. Withers – Henry Royce Institute, Department of Materials, School of Natural Sciences and The Royce Institute, Department of Materials, School of Natural Sciences, University of Manchester, Manchester M13 9PL, U.K.

K. J. Roberts – Centre for the Digital Design of Drug Products, School of Chemical and Process Engineering, University of Leeds, Leeds LS2 9JT, U.K.; orcid.org/0000-0002-1070-7435

Complete contact information is available at: <https://pubs.acs.org/10.1021/acs.cgd.9b01515>

Notes

The authors declare no competing financial interest.

■ ACKNOWLEDGMENTS

The authors would like to thank Dr. M. Ticehurst for his insightful discussions around the topic of powder flow and tableting of pharmaceutical materials. This work was funded by the Advanced Manufacturing Supply Chain Initiative 'Advanced Digital Design of Pharmaceutical Therapeutics' (ADDoPT) project (Grant No. 14060). This work also builds upon research on morphological modelling supported by EPSRC Grant EP/I028293/1 and the Synthonic Engineering programme supported by Pfizer, Boeringer-Ingellheim, Novartis, and Syngenta. P.G. also acknowledges funding support from EP/N025075/1. Beam time was funded through the Henry Royce Institute for Advanced Materials, funded through the Engineering and Physical Science Research Council (EPSRC) grants EP/R00661X/1, EP/S019367/1, EP/P025021/1, and EP/P025498/1, and performed at the Henry Moseley X-ray Imaging Facility, which was established through EPSRC grants EP/F007906/1, EP/F001452/1, EP/I02249X, EP/M010619/1, EP/F028431/1 and EP/M022498/1.

■ REFERENCES

- (1) Yu, L. X. Pharmaceutical quality by design: product and process development, understanding, and control. *Pharm. Res.* **2008**, *25*, 781–91.
- (2) Yu, L. X.; Amidon, G.; Khan, M. A.; Hoag, S. W.; Polli, J.; Raju, G. K.; Woodcock, J. Understanding pharmaceutical quality by design. *AAPS J.* **2014**, *16*, 771–83.
- (3) Bryant, M. J.; Rosbottom, I.; Bruno, I. J.; Docherty, R.; Edge, C. M.; Hammond, R. B.; Peeling, R.; Pickering, J.; Roberts, K. J.; Maloney, A. G. P. Particle Informatics": Advancing Our Understanding of Particle Properties through Digital Design. *Cryst. Growth Des.* **2019**, *19*, 5258–5266.
- (4) Simon, L. L.; Kiss, A. A.; Cornevin, J.; Gani, R. Process engineering advances in pharmaceutical and chemical industries: digital process design, advanced rectification, and continuous filtration. *Curr. Opin. Chem. Eng.* **2019**, *25*, 114–121.

- (5) Politis, S. N.; Colombo, P.; Colombo, G.; Rekkas, D. M. Design of experiments (DoE) in pharmaceutical development. *Drug Dev. Ind. Pharm.* **2017**, *43*, 889–901.
- (6) Train, D. An investigation into the compaction of powders. *J. Pharm. Pharmacol.* **1956**, *8*, 745–61.
- (7) Mihailidis, D. Computed Tomography From Photon Statistics to Modern Cone-Beam CT. *Med. Phys.* **2009**, *36*, 3858–3858.
- (8) Flannery, B. P.; Deckman, H. W.; Roberge, W. G.; D'Amico, K. L. Three-Dimensional X-ray Microtomography. *Science* **1987**, *237*, 1439–44.
- (9) Wellington, S. L.; Vinegar, H. J. X-Ray Computerized Tomography. *JPT, J. Pet. Technol.* **1987**, *39*, 885–898.
- (10) Cormack, A. M. Representation of a Function by Its Line Integrals, with Some Radiological Applications. *J. Appl. Phys.* **1963**, *34*, 2722–2727.
- (11) Fu, X.; Elliott, J. A.; Bentham, A. C.; Hancock, B. C.; Cameron, R. E. Application of X-ray Microtomography and Image Processing to the Investigation of a Compacted Granular System. *Particle & Particle Systems Characterization* **2006**, *23*, 229–236.
- (12) Sinka, I. C.; Burch, S. F.; Tweed, J. H.; Cunningham, J. C. Measurement of density variations in tablets using X-ray computed tomography. *Int. J. Pharm.* **2004**, *271*, 215–24.
- (13) Smith, C. J.; Stephens, J. D.; Hancock, B. C.; Vahdat, A. S.; Cetinkaya, C. Acoustic assessment of mean grain size in pharmaceutical compacts. *Int. J. Pharm.* **2011**, *419*, 137–46.
- (14) Busignies, V.; Leclerc, B.; Porion, P.; Evesque, P.; Couarraze, G.; Tchoreloff, P. Quantitative measurements of localized density variations in cylindrical tablets using X-ray microtomography. *Eur. J. Pharm. Biopharm.* **2006**, *64*, 38–50.
- (15) Yost, E.; Chalus, P.; Zhang, S.; Peter, S.; Narang, A. S. Quantitative X-Ray Microcomputed Tomography Assessment of Internal Tablet Defects. *J. Pharm. Sci.* **2019**, *108*, 1818–1830.
- (16) Garner, S.; Ruiz, E.; Strong, J.; Zavaliangos, A. Mechanisms of crack formation in die compacted powders during unloading and ejection: An experimental and modeling comparison between standard straight and tapered dies. *Powder Technol.* **2014**, *264*, 114–127.
- (17) Hancock, B. C.; Mullarney, M. P. X-ray microtomography of solid dosage forms. *Pharm. Technol.* **2005**, *29*, 92–100.
- (18) Merkle, A. P.; Gelb, J. The Ascent of 3D X-ray Microscopy in the Laboratory. *Microsc. Today* **2013**, *21*, 10–15.
- (19) Gajjar, P.; Styliari, I.D.; Nguyen, T.T.H.; Carr, J.; Chen, X.; Elliott, J.A.; Hammond, R.B.; Burnett, T.L.; Roberts, K.; Withers, P.J.; Murnane, D. 3D Characterisation of Dry Powder Inhaler Formulations: Developing X-ray Micro Computed Tomography Approaches. *Eur. J. Pharm. Biopharm.* **2020**, *151*, 32–44.
- (20) Jacques, S. D. M.; Pile, K.; Barnes, P.; Lai, X.; Roberts, K. J.; Williams, R. A. An In-Situ Synchrotron X-ray Diffraction Tomography Study of Crystallization and Preferred Crystal Orientation in a Stirred Reactor. *Cryst. Growth Des.* **2005**, *5*, 395–397.
- (21) Pile, K.; Lai, X.; Jacques, S. D. M.; Roberts, K. J.; Barnes, P. An investigation of crystallite alignment and polymorphic interaction of glutamic acid using an in situ synchrotron X-ray diffraction tomographic technique. *J. Cryst. Growth* **2006**, *294*, 41–45.
- (22) Wang, Y.; Wertheim, D. F.; Jones, A. S.; Coombes, A. G. Micro-CT in drug delivery. *Eur. J. Pharm. Biopharm.* **2010**, *74*, 41–9.
- (23) Hindelang, F.; Zurbach, R.; Roggo, Y. Micro Computer Tomography for medical device and pharmaceutical packaging analysis. *J. Pharm. Biomed. Anal.* **2015**, *108*, 38–48.
- (24) Losi, E.; Peppas, N. A.; Ketcham, R. A.; Colombo, G.; Bettini, R.; Sonvico, F.; Colombo, P. Investigation of the swelling behavior of Dome Matrix drug delivery modules by high-resolution X-ray computed tomography. *J. Drug Delivery Sci. Technol.* **2013**, *23*, 165–170.
- (25) Wray, P.; Chan, K. L.; Kimber, J.; Kazarian, S. G. Compaction of pharmaceutical tablets with different polymer matrices studied by FTIR imaging and X-ray microtomography. *J. Pharm. Sci.* **2008**, *97*, 4269–77.
- (26) Kitamura, M. Polymorphism in the crystallization of L-glutamic acid. *J. Cryst. Growth* **1989**, *96*, 541–546.
- (27) Kitamura, M. Controlling factor of polymorphism in crystallization process. *J. Cryst. Growth* **2002**, *237*, 2205–2214.
- (28) Cornel, J.; Lindenberg, C.; Mazzotti, M. Experimental characterization and population balance modeling of the polymorph transformation of L-glutamic acid. *Cryst. Growth Des.* **2009**, *9*, 243–252.
- (29) Dharmayat, S.; De Anda, J. C.; Hammond, R. B.; Lai, X.; Roberts, K. J.; Wang, X. Z. Polymorphic transformation of l-glutamic acid monitored using combined on-line video microscopy and X-ray diffraction. *J. Cryst. Growth* **2006**, *294*, 35–40.
- (30) Ferrari, E. S.; Davey, R. J. Solution-mediated transformation of α to β L-glutamic acid: Rate enhancement due to secondary nucleation. *Cryst. Growth Des.* **2004**, *4*, 1061–1068.
- (31) Ono, T.; Kramer, H.; Ter Horst, J.; Jansens, P. Process modeling of the polymorphic transformation of L-glutamic acid. *Cryst. Growth Des.* **2004**, *4*, 1161–1167.
- (32) Ono, T.; Ter Horst, J.; Jansens, P. Quantitative measurement of the polymorphic transformation of L-glutamic acid using in-situ Raman spectroscopy. *Cryst. Growth Des.* **2004**, *4*, 465–469.
- (33) Hammond, R.; Pencheva, K.; Roberts, K. Simulation of energetic stability of faceted L-glutamic acid nanocrystalline clusters in relation to their polymorphic phase stability as a function of crystal size. *J. Phys. Chem. B* **2005**, *109*, 19550–19552.
- (34) Hammond, R. B.; Pencheva, K.; Roberts, K. J. Structural variability within, and polymorphic stability of, nano-crystalline molecular clusters of l-glutamic acid and D-mannitol, modelled with respect to their size, shape and 'crystallisability'. *CrystEngComm* **2012**, *14*, 1069–1082.
- (35) Leane, M.; Pitt, K.; Reynolds, G. A proposal for a drug product Manufacturing Classification System (MCS) for oral solid dosage forms. *Pharm. Dev. Technol.* **2015**, *20*, 12–21.
- (36) Leane, M.; Pitt, K.; Reynolds, G. K.; Dawson, N.; Ziegler, I.; Szepes, A.; Crean, A. M.; Dall Agnol, R.; The Manufacturing Classification System (MCS) Working Group. Manufacturing classification system in the real world: factors influencing manufacturing process choices for filed commercial oral solid dosage formulations, case studies from industry and considerations for continuous processing. *Pharm. Dev. Technol.* **2018**, *23*, 964–977.
- (37) Goyal, A.; Sharma, V.; Sihag, M. K.; Tomar, S. K.; Arora, S.; Sabikhi, L.; Singh, A. K. Development and physico-chemical characterization of microencapsulated flaxseed oil powder: A functional ingredient for omega-3 fortification. *Powder Technol.* **2015**, *286*, 527–537.
- (38) Ferrari, E. S.; Davey, R. J. Solution-Mediated Transformation of α to β l-Glutamic Acid: Rate Enhancement Due to Secondary Nucleation. *Cryst. Growth Des.* **2004**, *4*, 1061–1068.
- (39) Cashell, C.; Corcoran, D.; Hodnett, B. K. Secondary nucleation of the beta-polymorph of L-glutamic acid on the surface of alpha-form crystals. *Chem. Commun. (Cambridge, U. K.)* **2003**, 374–5.
- (40) Hammond, R. B.; Pencheva, K.; Roberts, K. J. Molecular Modeling of Crystal–Crystal Interactions between the α - and β -Polymorphic Forms of l-Glutamic Acid Using Grid-Based Methods. *Cryst. Growth Des.* **2007**, *7*, 875–884.
- (41) Turner, T. D.; Caddick, S.; Hammond, R. B.; Roberts, K. J.; Lai, X. Kinetics of the Aqueous-Ethanol Solution Mediated Transformation between the Beta and Alpha Polymorphs of p-Aminobenzoic Acid. *Cryst. Growth Des.* **2018**, *18*, 1117–1125.
- (42) McDonald, S. A.; Reischig, P.; Holzner, C.; Lauridsen, E. M.; Withers, P. J.; Merkle, A. P.; Feser, M. Non-destructive mapping of grain orientations in 3D by laboratory X-ray microscopy. *Sci. Rep.* **2015**, *5*, 14665.
- (43) Yusop, S. N. A. *Characterisation of the Morphological and Surface Properties of Organic Micro-Crystalline Particles*; University of Leeds, 2014.
- (44) Krok, A.; Wu, C.-Y. Finite Element Modeling of Powder Compaction. In *Engineering Crystallography: From Molecule to Crystal*

to *Functional Form*; Roberts, K. J.; Docherty, R.; Tamura, R., Eds.; Springer Netherlands: Dordrecht, 2017; pp 451–462.

(45) Pei, C.; Wu, C.-Y. DEM Analysis of the Effects of Die Shape and Orientation on Die Filling Processes. In *Engineering Crystallography: From Molecule to Crystal to Functional Form*, Roberts, K. J.; Docherty, R.; Tamura, R., Eds.; Springer Netherlands: Dordrecht, 2017; pp 437–449.

(46) Jia, X.; Gan, M.; Williams, R. A.; Rhodes, D. Validation of a digital packing algorithm in predicting powder packing densities. *Powder Technol.* **2007**, *174*, 10–13.

(47) Caulkin, R.; Jia, X.; Xu, C.; Fairweather, M.; Williams, R. A.; Stitt, H.; Nijemeisland, M.; Aferka, S.; Crine, M.; Leonard, A.; Toye, D.; Marchot, P. Simulations of Structures in Packed Columns and Validation by X-ray Tomography. *Ind. Eng. Chem. Res.* **2009**, *48*, 202–213.

(48) Moreno-Atanasio, R.; Williams, R. A.; Jia, X. Combining X-ray microtomography with computer simulation for analysis of granular and porous materials. *Particuology* **2010**, *8*, 81–99.

(49) Gajjar, P.; Jorgensen, J. S.; Godinho, J. R. A.; Johnson, C. G.; Ramsey, A.; Withers, P. J. New software protocols for enabling laboratory based temporal CT. *Rev. Sci. Instrum.* **2018**, *89*, 093702.

(50) Van Snick, B.; Holman, J.; Cunningham, C.; Kumar, A.; Vercruyse, J.; De Beer, T.; Remon, J. P.; Vervaet, C. Continuous direct compression as manufacturing platform for sustained release tablets. *Int. J. Pharm.* **2017**, *519*, 390–407.

(51) Singh, R.; Velazquez, C.; Sahay, A.; Karry, K. M.; Muzzio, F. J.; Ierapetritou, M. G.; Ramachandran, R. Advanced Control of Continuous Pharmaceutical Tablet Manufacturing Processes. In *Process Simulation and Data Modeling in Solid Oral Drug Development and Manufacture*; Ierapetritou, M. G., Ramachandran, R., Eds.; Springer New York: New York, NY, 2016; pp 191–224.